The Astronomical Journal, 152:142 (8pp), 2016 November doi:10.3847/0004-6256/152/5/142

SPITZER SPACE TELESCOPE MID-IR LIGHT CURVES OF NEPTUNE

John Stauffer[1], Mark S. Marley[2], John E. Gizis[3], Luisa Rebull[1,4], Sean J. Carey[1], Jessica Krick[1], James G. Ingalls[1], Patrick Lowrance[1], William Glaccum[1], J. Davy Kirkpatrick[5], Amy A. Simon[6], and Michael H. Wong[7]

[1] Spitzer Science Center (SSC), California Institute of Technology, Pasadena, CA 91125, USA
[2] NASA Ames Research Center, Space Sciences and Astrobiology Division, MS245-3, Moffett Field, CA 94035, USA
[3] Department of Physics and Astronomy, University of Delaware, Newark, DE 19716, USA
[4] Infrared Science Archive (IRSA), 1200 E. California Boulevard, MS 314-6, California Institute of Technology, Pasadena, CA 91125, USA
[5] Infrared Processing and Analysis Center, MS 100-22, California Institute of Technology, Pasadena, CA 91125, USA
[6] NASA Goddard Space Flight Center, Solar System Exploration Division (690.0), 8800 Greenbelt Road, Greenbelt, MD 20771, USA
[7] University of California, Department of Astronomy, Berkeley CA 94720-3411, USA

Received 2016 July 13; revised 2016 August 12; accepted 2016 August 15; published 2016 October 27

ABSTRACT

We have used the *Spitzer Space Telescope* in 2016 February to obtain high cadence, high signal-to-noise, 17 hr duration light curves of Neptune at 3.6 and 4.5 μm. The light curve duration was chosen to correspond to the rotation period of Neptune. Both light curves are slowly varying with time, with full amplitudes of 1.1 mag at 3.6 μm and 0.6 mag at 4.5 μm. We have also extracted sparsely sampled 18 hr light curves of Neptune at W1 (3.4 μm) and W2 (4.6 μm) from the *Wide-feld Infrared Survey Explorer* (*WISE*)/*NEOWISE* archive at six epochs in 2010–2015. These light curves all show similar shapes and amplitudes compared to the *Spitzer* light curves but with considerable variation from epoch to epoch. These amplitudes are much larger than those observed with *Kepler*/*K*2 in the visible (amplitude ~0.02 mag) or at 845 nm with the *Hubble Space Telescope* (*HST*) in 2015 and at 763 nm in 2016 (amplitude ~0.2 mag). We interpret the *Spitzer* and *WISE* light curves as arising entirely from reflected solar photons, from higher levels in Neptune's atmosphere than for *K*2. Methane gas is the dominant opacity source in Neptune's atmosphere, and methane absorption bands are present in the *HST* 763 and 845 nm, *WISE* W1, and *Spitzer* 3.6 μm filters.

Key words: planets and satellites: individual (Neptune)

Supporting material: machine-readable tables

1. INTRODUCTION

Cloud formation in cool atmospheres is a key characteristic of planetary, exoplanetary, and brown dwarf atmospheres (Marley et al. 2013). We know from the study of isolated, self-luminous, field brown dwarfs that these clouds will typically not be completely uniform, but instead can have both vertical and horizontal structure, and vary in time. Synoptic monitoring of objects with patchy clouds is a powerful tool to study such objects because each observation samples different regions of the surface as the target rotates. Spectroscopic monitoring of brown dwarfs with the *Hubble Space Telescope* (*HST*) has detected wavelength dependent phase shifts in light curve features (Buenzli et al. 2012; Apai et al. 2013), best interpreted as due to molecules condensing at different pressure levels within the atmosphere and cloud structures in the vertical as well as horizontal (Buenzli et al. 2012; Yang et al. 2016), including in some cases the presence of a low pressure haze layer (Yang et al. 2015). The chemistry of the clouds varies with the temperature of the brown dwarf photosphere, from the warmest condensates (e.g., various oxides of magnesium and calcium) at $T_{\rm eff} \sim 2500$ K to water clouds for the coolest brown dwarfs (Faherty et al. 2014; Luhman & Esplin 2016). Using the *Spitzer Space Telescope* (Werner et al. 2004) to obtain mid-infrared time series photometry, Metchev et al. (2015) found that discrete cloud spots are present in most L and T-type brown dwarfs, typically producing variability in the range 0.2%–5%. Even higher amplitude variability is a characteristic of the L/T transition (Radigan 2014) where cloud properties change dramatically in a narrow temperature range. Cloud lifetimes apparently vary from hours (Gillon et al. 2013; Metchev et al. 2015) to years in some cases (Gizis et al. 2015). Cushing et al. (2016) found that a ~400K Y dwarf was variable at the 3.5% level, with the clouds changing in the months between observing epochs.

Extending this work to planetary-mass objects orbiting brighter primaries is challenging, but cloud variability in 2M1207b has been detected (Zhou et al. 2016) and the HR 8799 planets are being monitored (Apai et al. 2016). Extensive studies of this nature likely must await the *James Webb Space Telescope* or other future technologies. However, extending this work to the gas giants of the Solar System is possible now. And, while the surfaces of brown dwarfs and exoplanets cannot be spatially resolved, imaging of the gas giants in the Solar System is possible and can provide ground truth for inferences drawn from synoptic monitoring. Therefore, synoptic monitoring observations of Solar System planets as "point sources" provide a useful comparison to these brown dwarf and exoplanet results, as well as offering new insights into weather on the planets themselves. Although there is an exceptional long-term optical *b* and *y* band photometric sequence for Neptune (Lockwood et al. 1991) exhibiting variations in reflected light of a few percent over time, until fairly recently there has been little in the way of intensive, short term photometric monitoring of Solar System giant planets reported in the literature. Most recently Sromovsky et al. (2001) monitored Neptune over about one rotation period in 1996 from *HST* and measured variability as large as 22% at wavelengths with strong methane absorption. They attributed the variability to patchy, high altitude clouds. Much longer term cloud morphology changes for Neptune—over years—can be found in Karkoschka (2011) and Irwin et al. (2016),

who report that near-infrared high resolution imaging detects significant cloud evolution between 2009 and 2013.

The repurposed *Kepler*/*K*2 Mission (Howell et al. 2014) notably altered the status quo by providing the opportunity to obtain a continuous, months-long lightcurve of Neptune in a single broad optical band (0.43–0.90 μm). Neptune was observed by *K*2 in late 2014 at a one-minute cadence for 49 days (J. F. Rowe et al. 2016, in preparation). This *K*2 broadband optical light curve of Neptune is sensitive to light reflected from the planet and not thermal emission from the atmosphere. Thus the measured time-varying lightcurve is particularly sensitive to the scattering properties and altitudes of clouds within the atmosphere and the relative altitude of the clouds compared to other sources of atmospheric opacity, primarily methane absorption.

Simon et al. (2016) analyzed the cloud contributions to the complex Neptune *K*2 light curve. The light curve has an amplitude of ~2% and is dominated by discrete cloud features which are more (or less) reflective than the global cloud deck. Because of Neptune's latitude-dependent high winds, periods from 15 to 19 hr are detected instead of a single rotation period. The most significant periodic ($P = 16.8$ hr) signal is attributed to a single, long-lived stable feature at a latitude of 45° S. This bright cloud was confirmed by contemporaneous near-infrared Keck Adaptive Optics imaging and later *HST* optical imaging. Contributions from smaller, rapidly evolving discrete clouds add irregularities to the dominant signal.

At Jupiter, the transition from reflected sunlight dominating the disk-averaged emission to thermal emission takes place around 4 μm. The planet's famed five-micron hot spots, for example, are regions of thermal emission from the deep atmosphere pouring out through holes in the water and ammonia cloud decks in a region of low gas opacity. Large horizontal inhomogeneity at 5 μm corresponds to variability in the tropospheric weather layer. At the much colder Uranus and Neptune, the transition from scattered to emitted light takes place at longer wavelengths, at about 6–7 μm, and the thermal emission originates from the higher-altitude, radiatively controlled stratosphere. Examples of ice giant variability studies at thermal wavelengths include the work of Hammel et al. (2007) who detected a bright polar region at 7.7 and 11.7 μm in Neptune, and showed that these stratospheric ethane and methane emission features are uncorrelated with the deeper cloud features observed in near-infrared imaging. Based on independent, mid-IR ground-based imaging, Orton et al. (2007) detected a distinct rotating hot spot in ethane and methane emission; Orton et al. (2012) showed that this feature has been absent in some years and may be a wave feature excited by dynamics lower in the atmosphere.

In this paper, we provide the first well-sampled mid-infrared (mid-IR) light curves for Neptune based on thirty-five hours of continuous monitoring in early 2016 with *Spitzer*. We also provide six sparsely sampled mid-IR light curves of Neptune obtained in 2010 through 2015 with the *Wide-field Infrared Survey Explorer* (*WISE*; Wright et al. 2010) satellite. While these light curves are also sensitive to reflected light, they probe different depths into Neptune's cloudy atmosphere than those obtained previously with *K*2 and *HST*. Our data thereby add new constraints on the composition and structure or Neptune's cloud deck. Section 2 describes the various sources of data we use; Sections 3 and 4 describe in detail the analysis steps used to construct the *Spitzer* and *WISE* light curves. Section 5 compares the infrared light curves to those obtained at shorter wavelengths and the initial inferences we draw from these comparisons.

2. OBSERVATIONAL DATA

2.1. Spitzer Data

Neptune was observed between UT 2016 February 21–23 in both of the 3.6 μm (IRAC-1) and 4.5 μm (IRAC-2) channels of the Infrared Array Camera (IRAC; Fazio et al. 2004) on *Spitzer*. The measurements were part of Director's Discretionary Time Program 12125 (PI: Stauffer).

The time period was chosen expressly because Neptune as seen from *Spitzer* was near the stationary point in its orbit, thus minimizing the planet's motion during the many hour observation and thereby minimizing any possible time-varying contamination from background field stars that would pass through the Neptune or sky aperture for the photometry.

The Astronomical Observation Requests (AORs) were made in IRAC's staring mode, where for each channel, the spacecraft is maneuvered so that the target is placed on the well-calibrated peak-up pixel and back-to-back frames taken for the total time of the AOR with no dithering. For each channel, the total duration of the AOR was set to cover a complete rotation of Neptune, or about 17.2 hr. In channel 1 (3.6 μm), frames with times of 100 s were used (corresponding to 96.8 s exposure times), resulting in 622 images; in channel 2 (4.5 μm), a frametime of 30 s was used (corresponding to 26.8 s exposure times), resulting in 2018 images. The image files were dark-subtracted, linearized, flat-fielded, and calibrated using the S19.2 version of the IRAC pipeline. We had requested that the channel 2 observations be made immediately following the channel 1 observations, but a time-critical exoplanet transit observation was inserted between the two Neptune AORs, resulting in the channel 2 light curve beginning about 2.3 days after the start of the channel 1 observation.

Flux densities were measured with aperture photometry on the *Spitzer* Basic Calibrated Data images. After first determining the center of Neptune via a "center of light" technique (Ingalls et al. 2016), the flux was integrated over a 5 pixel radius aperture using the IDL Astronomy User's Library routine `aper.pro`.[8] The per-pixel average background was derived for each image using an annulus centered on Neptune with inner and outer radii of (16, 18) pixels. This per-pixel bias was scaled to the aperture area and subtracted from the integrated flux. Normally, a tighter annulus is used to derive the background for point source photometry but avoiding Triton and a background star required a minimum radius of 16 pixels. We corrected the fluxes for losses due to a finite aperture size by multiplying by the aperture corrections: 1.049 at 3.6 μm and 1.050 at 4.5 μm. These corrections were derived for point source observations with post-cryogenic IRAC for an aperture of 5 pixels radius and a background annulus of (10, 20) pixels. Simulations with the IRAC Point Response Function (PRF)[9] show that using a nonstandard (16, 18) background annulus changes the flux by only 0.2% compared to the (10, 20) annulus. However, these aperture corrections were not optimized for non-point objects (Neptune's angular diameter from Earth ranges from 2.″17 to 2.″37, whereas the IRAC

[8] http://idlastro.gsfc.nasa.gov/ftp/pro/idlphot/aper.pro

[9] http://irsa.ipac.caltech.edu/data/SPITZER/docs/irac/calibrationfiles/psfprf/

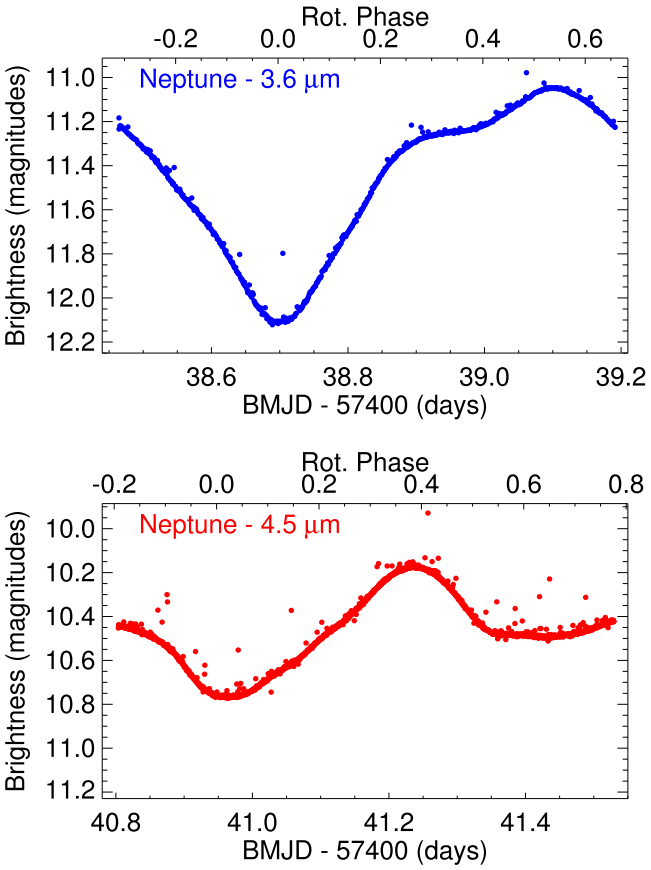

Figure 1. *Spitzer* light curves of Neptune from 2016 February, in the 3.6 μm (top) and 4.5 μm (bottom) bands of IRAC. Vertical scales of both plots cover a range of 1.4 mag. Upper axes indicate rotational phase, derived using a period of 18 hr and defining zero phase at the time of the 3.6 μm minimum.

point-spread function (PSF) at 3.6 and 4.5 μm is about 1.″8 FWHM). We expect therefore some unaccounted-for aperture losses which do not affect relative flux estimates. Additional losses due to the under-sampled PSF and a variable spatial response of each pixel (the so-called "pixel-phase effect"), *can* affect relative flux variations when coupled with normal spacecraft pointing fluctuations. However, the magnitude of this effect is only a few percent (about one tick mark in Figure 1; see Ingalls et al. 2012) for point sources and less for partially resolved sources like Neptune, and so we did not attempt to correct for it here.

We converted aperture fluxes to magnitudes using the in-band flux densities of Vega: 278 Jy (3.6 μm) and 180 Jy (4.5 μm). The fluxes reported for both IRAC and *WISE* are not color corrected for the difference between the spectral energy distribution of Neptune and the fiducial spectral shape $F_\nu \propto \nu^{-1}$ used in the calibration of IRAC (Reach et al. 2005), or the $F_\nu \propto \nu^{-2}$ adopted for the calibration of *WISE* (Wright et al. 2010). Not attempting a color correction should not affect the measured color variation unless the underlying spectral energy distribution is also varying significantly. For a detailed color comparison between the IRAC and *WISE* data, a spectral energy distribution must be assumed and color corrections applied to account for the different bandpass profiles and the different calibration assumptions.

2.2. *WISE* Data

WISE was launched on 2009 December 14 to survey the sky in four broad wavelength bands referred to as W1 (3.4 μm), W2 (4.6 μm), W3 (12 μm), and W4 (22 μm). After an in-orbit checkout, *WISE* began surveying the sky on 2010 January 14 in a Sun-synchronous polar orbit around the Earth, allowing the entire sky to be mapped in just six months. Along the ecliptic, each location is visited a minimum of eight times during each sky pass, and each of those visits has an exposure time of 7.7 s at W1 and W2 and 8.8 s at W3 and W4. Those data are generally confined to a ~24 hr period since the observatory sweeps through roughly one degree in ecliptic longitude per day. Exceptions to this are when the scan track is temporarily toggled to either larger or smaller longitudes in order to avoid the boresight's passing within five degrees of the moon. In such cases, observations of a particular sky location may be interrupted by a couple of days while the moon passes, in which case the coverage at that epoch may be spread over a few days surrounding the gap.

WISE completed its first full pass of the sky on 2010 July 17. On 2010 August 05, during the second pass, the outer, secondary tank was depleted of its cryogen, rendering the W4 band unusable. This was followed by depletion of cryogen from the inner, primary tank on 2010 September 30, which rendered the W3 band unusable. The two short-wavelength bands were largely unaffected, so *WISE* continued to collect data in W1 and W2 until the spacecraft was placed into hibernation on 2011 January 31, having then completed two full sky passes and 20% of a third. *WISE* observations resumed in 2013 December as the re-branded *NEOWISE* mission, which is scheduled to map the sky six additional times. *NEOWISE* observations will continue through the end of 2016.

The W1 band has a central wavelength designed to fall in the middle of the strong 3.3 μm fundamental methane absorption band seen in colder brown dwarfs and giant planets. The W2 band has a central wavelength of 4.6 μm, where the atmospheres of these objects are relatively transparent to radiation, assuming a cloud-free atmosphere. An example is the 5 μm region in the atmosphere of Jupiter, where thermal emission can be seen through holes in the thick cloud layer (Westphal 1969). These two bandpasses therefore can sample two very different physical regimes in the atmospheres of these objects and can be used to study their chemistry and physics (see Figure 2 of Mainzer et al. 2011).

As can be gleaned from the *WISE* bandpass coverages shown in Figure 7 of Wright et al. (2010) and the *Spitzer*/Infrared Spectrograph spectra of known brown dwarfs in Figure 5 of Cushing et al. (2006), the W3 band samples a wavelength regime including CH_4 and NH_3 absorption troughs. The W4 band, however, samples a region of the Rayleigh–Jeans tail with no sharp, deep molecular absorption bands, at least as predicted by brown dwarf atmospheric models (Burrows et al. 2003).

Neptune has been observed at six different epochs in the currently available *WISE* and *NEOWISE* data releases. Its magnitudes range from W1 $\approx$ 10.1–11.5 mag, W2 $\approx$ 9.5–11.1 mag, W3 $\approx$ 2.8–3.1 mag, and W4 $\approx$ 0.0–0.3 mag. As stated in the *WISE* All-Sky Release Explanatory Supplement (Cutri et al. 2012), the detectors saturate at W1, W2, W3, and W4 magnitudes of 8.1, 6.7, 3.8, and −0.4 mag, respectively. The profile-fit photometric measurements can extend the usable

range to brighter magnitudes by using the non-saturated wings of the stellar profile, and this extends *WISE* photometric measurements to W1, W2, W3, and W4 levels of 2.0, 1.5, −3.0, and −4.0 mag, respectively. Because the measured magnitudes for Neptune are fainter than these limits—and because the apparent size of Neptune (∼2.″2) is far less than the *WISE* resolution (6.″1, 6.″4, 6.″5, and 12.″0 in W1 through W4, respectively)—the profile-fit photometry listed for Neptune in the *WISE* Single Exposure Source Data Bases should be of good quality.

2.3. *HST* Imaging

HST is capable of providing images of with spatial resolution of Neptune's atmosphere ∼1000–2000 km, thus providing dozens of resolution elements over Neptune's 50,000 km diameter. Although *HST* imaging was not obtained at the same time as the *Spitzer* data, global Neptune maps were obtained in 2015 September as part of the Hubble Outer Planet Atmospheres Legacy (OPAL) program (Simon et al. 2016, Figure 5). These maps were obtained in multiple filters, allowing direct viewing of the current cloud features, but with coarse temporal spacing. All filters redward of 600 nm show similar cloud features, with good contrast against the background atmosphere. The filter used most often, F845M, provides the best light curve for comparison with other data sets. A discrete storm system was visible throughout 2015 near 45° S and dominated the Hubble (16% peak-to-trough variation at 845 nm) and 49 day *Kepler* lightcurves (2% peak-to-trough variation) (Simon et al. 2016).

This bright cloud feature at 45° S was suspected to be a bright companion cloud to an unseen dark vortex, similar to the Great Dark Spot seen by *Voyager 2* (Smith et al. 1989). The 2015 *HST* observations indeed detected a dark feature at blue wavelengths, which was confirmed by more recent Hubble imaging acquired on 2016 May 15 and 16 (Wong et al. 2016). The bright companion clouds were again present in the 2016 observations, strongly suggesting that they were still present during the *Spitzer* observations, though at that time, Neptune was too close to the Sun for ground-based verification. Another large bright storm system was also present in the 2016 data between 15 and 45° S and was the brightest feature on the planet. This data set was not optimized for temporal sampling, with only 4 views over the course of 27.5 hr. At 763 nm, Neptune again showed variations of about 0.2 mag due to the larger cloud system.

3. *SPITZER* LIGHT CURVES

We display light curves of Neptune measured with *Spitzer*/IRAC in Figure 1. The light curve data are provided in tabular form in Tables 1 and 2. These are the first continuous Neptune light curves covering a full rotation at mid-IR wavelengths. The amplitude at 3.6 μm is 1.06 mag, corresponding to a peak-to-trough flux variation of more than a factor of 2.5; at 4.5 μm the amplitude is 0.59 mag, corresponding to a peak-to-trough flux variation of about 1.7. These are consistent with the amplitudes measured in the similar passbands *WISE* W1 and W2, respectively (see below), but are much larger than the amplitudes of the *K*2 0.65 μm lightcurve of 2015 January (∼2%; Simon et al. 2016), as well as the *HST* 845 nm measurements (16%).

Table 1
Spitzer 3.6 μm Light Curve for Neptune

BMJD[a] (days)	[3.6] (mag)	Uncertainty (mag)
57438.46455	11.1835	0.0063
57438.46470	11.2340	0.0018
57438.46587	11.2193	0.0018
57438.46704	11.2196	0.0020
57438.46821	11.2234	0.0020
57438.46938	11.2256	0.0020
57438.47055	11.2304	0.0020
57438.47172	11.2355	0.0019
57438.47288	11.2376	0.0019
57438.47406	11.2398	0.0018

Note.
[a] Barycentric Modified Julian Date at the start of the 100 s integration.
(This table is available in its entirety in machine-readable form.)

Table 2
Spitzer 4.5 μm Light Curve for Neptune

BMJD[a] (days)	[4.5] (mag)	Uncertainty (mag)
57440.80363	10.4527	0.0026
57440.80399	10.4387	0.0026
57440.80435	10.4371	0.0026
57440.80471	10.4451	0.0026
57440.80507	10.4385	0.0026
57440.80543	10.4420	0.0025
57440.80579	10.4441	0.0025
57440.80615	10.4416	0.0026
57440.80651	10.4423	0.0026
57440.80687	10.4431	0.0026

Note.
[a] Barycentric Modified Julian Date at the start of the 30 s integration.
(This table is available in its entirety in machine-readable form.)

We label the upper axes of Figure 1 in terms of rotational "phase," derived using a rotation rate of 18.0 hr, corresponding to zonal winds at ∼25° latitude (Smith et al. 1989; Hammel & Lockwood 2007). Assuming these observations bear the imprint of the brightest feature seen in the 2016 May *HST* images, an 18 hr period is the approximate mean of the two largest power spectral density peaks found in *K*2 data corresponding to zonal winds between 20° and 30° latitude (Simon et al. 2016, Figure 2). We define zero phase to occur at the approximate time of the 3.6 μm minimum, defined as the barycentric modified Julian date (BMJD) at the start of the 100 s 3.6 μm integration with the lowest flux, BMJD = 57438.697536 days. As seen in Figure 1, the 4.5 μm light curve obtains its minimum about 54 hr after the 3.6 μm curve, which is near phase zero under this definition. In other words, the 3.6 and 4.5 μm light curves exhibit minimum reflectance with a timing that is consistent with the rotational period of zonal winds at ∼25° latitude.

4. *WISE* LIGHT CURVES

Light curves at the *WISE* W1 and W2 bands are shown in Figure 2. The *WISE* data are provided in tabular form in Table 3. This photometry can be found in the Single Exposure Source Tables from the All-Sky, Post-Cryo, and NEOWISE-R

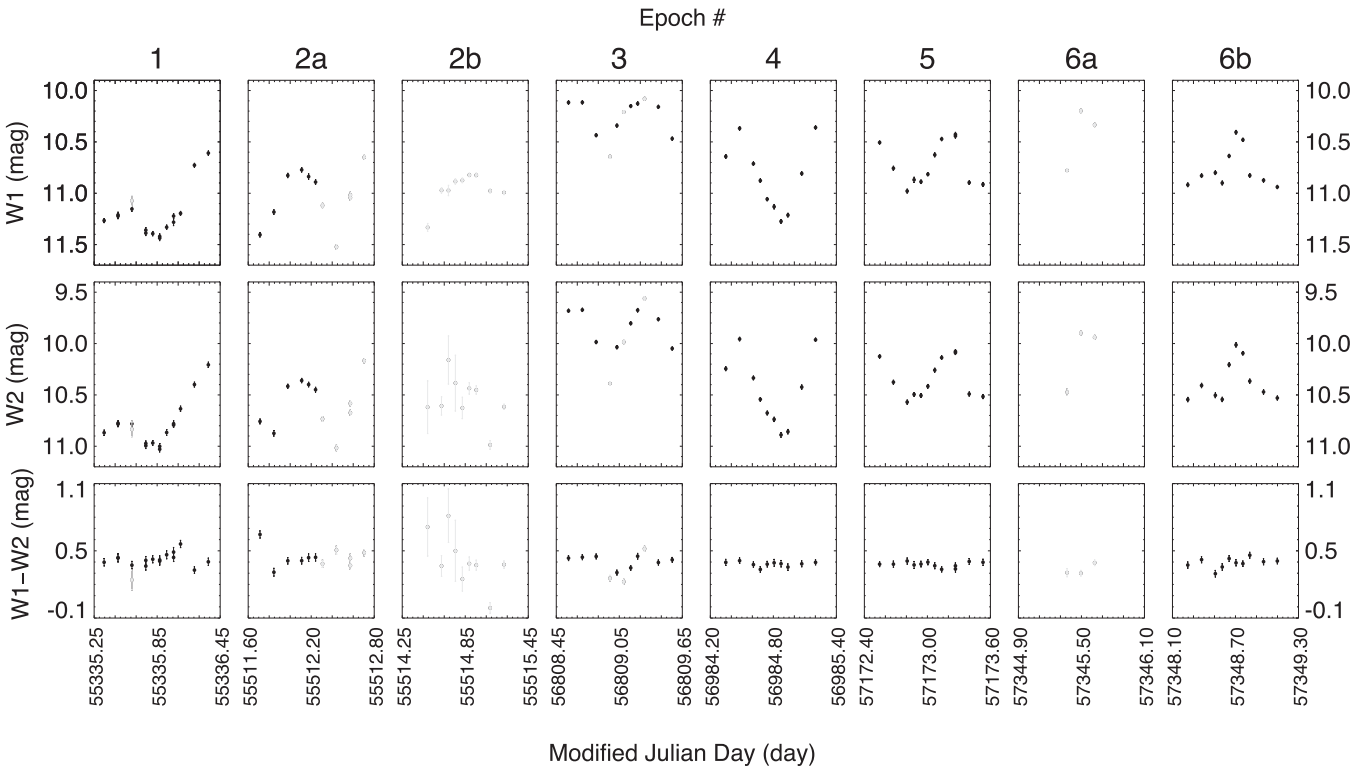

Figure 2. Light curves of Neptune using *WISE* W1 and W2 data. The top row shows the variation in W1 mag, the second row shows W2 mag, and the bottom row shows the W1−W2 color. Each column represents a different epoch, as defined in Table 4. For many of the data points shown, the symbol size is larger than the photometric uncertainties, so error bars are not visible. Points in black are those used in the statistics computed in Table 4. Points in light gray are ones that failed to meet our criteria for high-quality photometry. See text for details.

Table 3
WISE Light Curve Data for Neptune

MJD (days)	W1 (mag)	W1 Uncertainty (mag)	W2 (mag)	W2 Uncertainty (mag)
55335.345131	11.266	0.020	10.868	0.026
55335.477308	11.211	0.027	10.775	0.024
55335.477435	11.223	0.025	10.784	0.026
55335.609612	11.074	0.052	10.834	0.072
55335.609739	11.153	0.023	10.781	0.025
55335.741916	11.359	0.024	10.995	0.027
55335.742043	11.388	0.024	10.973	0.025

(This table is available in its entirety in machine-readable form.)

periods available through the NASA/IPAC Infrared Science Archive.[10] As shown in the figure, there are six epochs of data. For the second and sixth epochs, the usual ∼24 hr observing window was interrupted by a ∼2 day moon toggle, so data have been split into "a" and "b" subgroups.

We have performed quality analysis on the photometry. Unless otherwise stated, the data appear to be excellent. Where there are apparent issues, we discuss them in order of their epoch (where epoch numbers appear in Figure 2 and below in Table 4):

1. Epoch 1: The observation at MJD 55335.609 (specifically, the one with scan/frame ID 04717b151) has Neptune very close to an array edge, and the photometric uncertainties are correspondingly much higher than normal. This point has been removed from further analysis.
2. Epoch 2a: The last five observations at this epoch have moon mask flags indicating that they fall within the zone where moonlight can severely contaminate the W2 backgrounds; the last three observations have this same moon mask flag set for W1. A check of the images at these dates confirms high backgrounds in both bands. As a result, we have removed all five of these data points from subsequent analysis.
3. Epoch 2b: All of the data at this epoch are likely contaminated by moonlight in both W1 and W2, as indicated by the moon mask flag. The high photometric uncertainties for these points as well as a visual check of the images indicate that moonlight is indeed quite severe for the majority of these observations. All data at this epoch have been removed from subsequent analysis.
4. Epoch 3: The data for MJD values of 56808.960 (scan/frame ID 49349b151), 56809.092 (49353b151), and 56809.289 (49360a126) have image quality flags indicating streaked frames. These data points have been removed from further analysis.
5. Epoch 6a: All three data points have potential problems with high backgrounds due to moonlight, as indicated by the moon mask flag. The images confirm that the moonlight in these frames is severe. All three of these points have been removed from subsequent analysis.

For each epoch, Table 4 summarizes the mean magnitude and the amplitude of the variability in each band and in the [W1]−[W2] color. We note that the mean W1 and W2

[10] http://irsa.ipac.caltech.edu

Table 4
WISE Neptune Observation Log

Epoch #	MJD Range (day)	# of Meas. Total	# of Meas. Used	Mean W1 (mag)	Mean W2 (mag)	Mean W3 (mag)	Mean W4 (mag)	W1 Amp. (mag)	W2 Amp. (mag)	Mean W1−W2 (mag)	W1−W2 Amp. (mag)
1	55335.3–55336.4	16	15	11.21	10.79	3.02	0.19	0.83	0.82	0.42	0.20
2a	55511.7–55512.8	11	6	10.99	10.54	…	…	0.63	0.52	0.44	0.34
2b	55514.4–55515.3	9	0	…	…	…	…	…	…	…	…
3	56808.5–56809.6	11	8	10.24	9.84	…	…	0.35	0.38	0.41	0.15
4	56984.3–56985.3	10	10	10.84	10.46	…	…	0.91	0.93	0.38	0.08
5	57172.5–57173.6	12	12	10.72	10.34	…	…	0.55	0.49	0.38	0.07
6a	57345.3–57345.7	3	0	…	…	…	…	…	…	…	…
6b	57348.2–57349.1	10	10	10.76	10.37	…	…	0.53	0.53	0.39	0.17

Note. Epoch 1 is from the All-Sky phase of the mission, epoch 2 is from the Post-Cryo period, and epochs 3–6 are from the ongoing *NEOWISE* survey. Coverage of the field at epochs 2 and 6 was interrupted by a toggle of the spacecraft's scan path to avoid excessive moonlight.

magnitudes have changed by ∼1.0 mag between epoch 1 and epoch 3. Variations this large are sometimes also seen within an individual epoch, such as in epochs 1 and 4, with variations changing gradually on timescales similar to the *WISE* sampling of 90 minutes (Figure 2).

Despite the large excursions in W1 and W2 magnitude over the course of a single day, the [W1]−[W2] color remains relatively constant at ∼0.4 mag, although some excursions from this value, such as for the first data point at epoch 2a, are seen. This same value of [W1]−[W2] ≈ 0.4 mag also holds across the entire 5.5 years data set.

Simultaneous data at W3 and W4 also exist for epoch 1. At W3 band, the core of Neptune's PSF is saturated, and the reduced χ^2 values from the PSF-fit photometry are generally well above 1.0, indicating that the PSF fit was a poor match to the observed profile. Even though the W4 magnitude is fainter than the saturation limit, the reduced χ^2 values from the PSF fit are also much greater than 1.0. As a result, the quoted photometric errors in both bands are likely underestimated given that the photometric measurements themselves are likely biased. Since this makes interpretation of any real variability difficult, we quote only the mean W3 and W4 magnitudes in Table 4.

5. PHYSICAL INTERPRETATION

The IRAC-1 (3.6 μm) and IRAC-2 (4.5 μm) light curves look very similar to the light curves obtained by *K*2 and *Hubble* in 2014/2015, despite the difference in the amplitude of the variations, Figure 3, top panel. Figure 3 bottom panel illustrates this assertion, by over-plotting portions of the light curves from each facility, arbitrarily phase shifting their *x*-axis location so that the light-curve minima are aligned. These observations are nominally sensitive to a different altitude in the atmosphere. Figure 4 shows that, in a cloud-free atmosphere, each filter should be sensitive to different altitudes, with the IRAC-1 band most sensitive to stratospheric levels, similar to the *WISE* W1 (3.4 μm) filter.

However, if clouds and hazes lie above the point in the atmosphere where the column gas opacity becomes substantial (e.g., above the black curve in Figure 4), they can dominate reflectance. This leads to a flattening of the reflectance spectrum. In spatially resolved observations, limb and nadir observations can be combined to better constrain cloud heights by leveraging the different atmospheric columns (Simon & Beebe 1996). Likewise, in the forward scattering realm probed

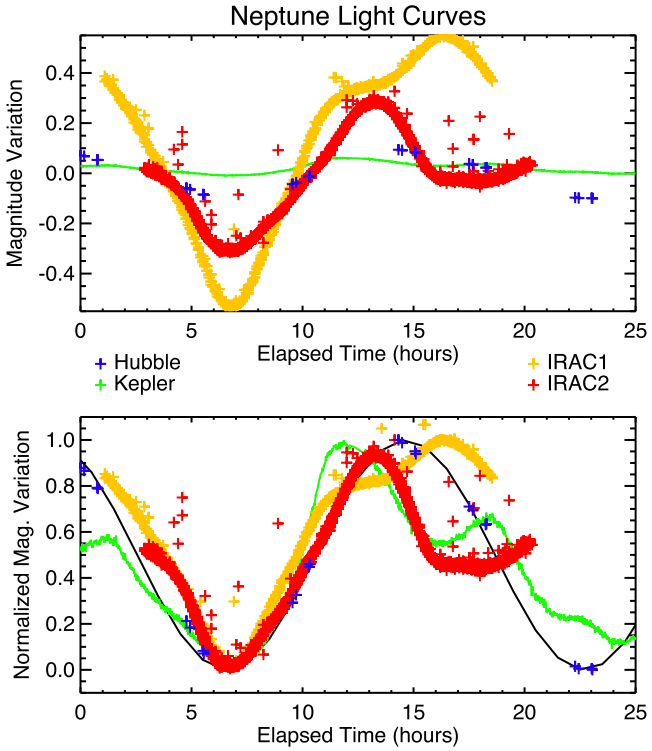

Figure 3. Normalized magnitude light curves of Neptune using *Hubble* 2015, *K*2 and *Spitzer* data. The top panel shows the magnitude variations from each facility, time-shifted to align their first minima and centered on their mean values, allowing comparison of light curve amplitudes. The bottom panel shows the same, but with the amplitude of the variations normalized between 0 and 1 to allow comparison of light curve shapes. The solid black line indicates Neptune's rotation period, with no adjustment for the planet's inclination.

by exoplanet transit observations, the longer path lengths near the limb allow even low-opacity hazes to strongly affect transmission spectra (Fortney 2005), eliminating detectable gas absorption bands in the atmospheres of, e.g., HD 189733b and GJ1214b (Pont et al. 2008; Bean et al. 2011; Berta et al. 2012).

In our disk integrated mid-IR lightcurves, we see little difference between the ∼3.6 and ∼4.5 μm channels, despite the large differences in methane opacity between the two bands. This implies that any cloud opacity must lie sufficiently high in the atmosphere that both bands see a comparable contribution. Judging from Figure 4, this suggests that optically thick clouds,

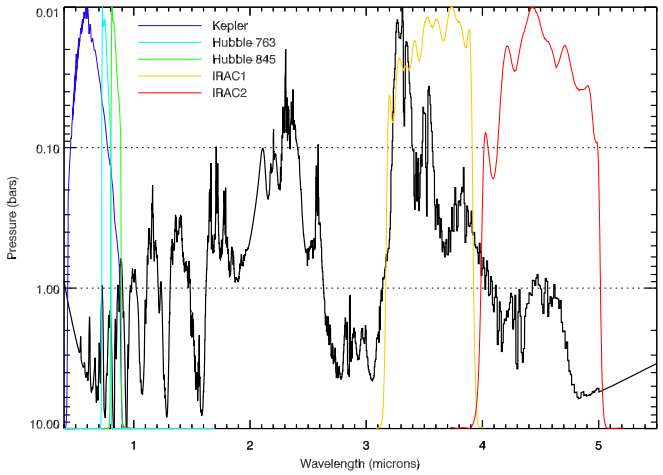

Figure 4. Atmospheric transmission for Neptune or Uranus (P. Irwin 2016, personal communication). The black line shows the approximate transmission level for 50% absorption in a cloud-free atmosphere, including Rayleigh scattering, $H_2 - H_2$ and $H_2 - He$ collision-induced absorption, and methane gas absorption. Filter bandpasses are shown by the colored lines. In a cloud-free atmosphere, each filter should be sensitive to different altitudes, with data near $\sim$3 μm most sensitive to stratospheric levels. Cloud layers overlying the indicated pressure level are visible in reflected light. We see no evidence that the IR bandpasses sampled clouds at different altitudes, which would manifest as different photometric amplitudes, a phase shift, or other significant morphological differences between lightcurves.

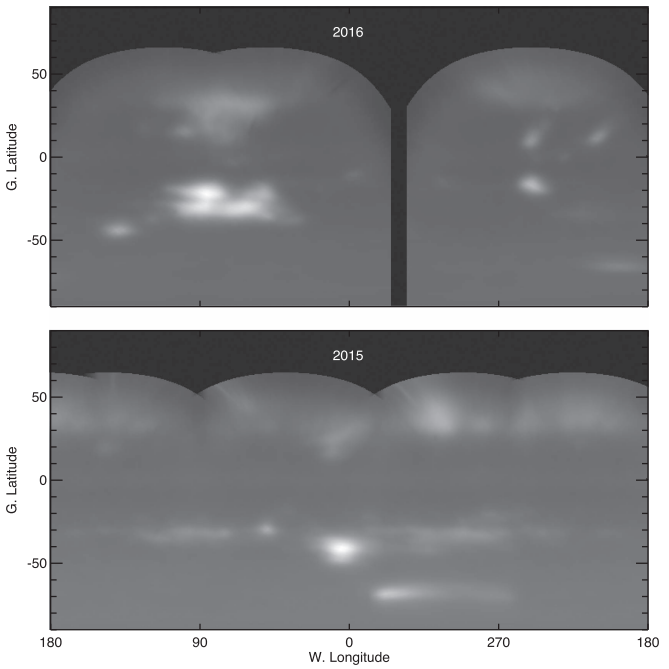

Figure 5. Hubble maps of Neptune at 763 nm. These data are rectilinear mapped at 0.5 deg pix^{-1} resolution and cover all latitudes and longitudes. Latitude coverage is incomplete due to Neptune's tilt. A gap in the 2016 longitude coverage is produced because two opposite hemispheres were imaged separately, about 24 hr apart. Patchy cloud features are visible at most longitudes, and they evolve rapidly from day to day.

or at least the cloudtops, must lie above about 0.30 bar. Further detailed modeling is required to refine this estimate.

Furthermore, we find little morphological differences between the two lightcurves. Differences in cloud evolution or wind speed as a function of altitude would manifest as different periods in the light curves. A variation in the wind speed with altitude is expected based on the 3D temperature field measured by *Voyager* (Conrath et al. 1991; Fletcher et al. 2014). Recent Keck observations have detected vertical windshear on Neptune by tracking resolved cloud features at two different infrared wavelengths (Tollefson et al. 2016), although the majority of discrete tracked features are too small and short-lived to create periodic photometric signals in the short duration lightcurve reported here. In general, the unresolved observations are sensitive to very large cloud systems with significant vertical range and uniform motion, producing similar lightcurves at all wavelengths studied.

Mapping the *Hubble* data at 763 nm from 2015 and 2016, Figure 5 shows that patchy cloud features are visible at most longitudes. These features evolve rapidly from day to day. In the 2015 data, the dominant feature was the cloud system near 45° S, while in 2016, it is the larger storm complex between 15 and 45° S. Although there is incomplete coverage, there are still clouds at most longitudes, such that a 763 or 845 nm light curve is still sensitive to features outside the largest storm system. However, if one only considers the brightness in the large bright cloud systems, compared with the darkest regions, the brightness varies by about 1.4 mag in 2015 and 1.7 mag in 2016 at 763 nm. Thus, the amplitudes of the light curves from the *Spitzer* and *WISE* filters are consistent with being most sensitive to the highest clouds against a dark background.

6. SUMMARY AND CONCLUSIONS

The synergy between Solar System and various brown dwarf and extrasolar planet cloud decks has been apparent for some time. Ackerman & Marley (2001) suggested for example that the L to T type transition in brown dwarfs might be associated with the appearance of regions of low cloud opacity, analogous to Jupiter's 5 μm hot spots. Many early searches for brown dwarf variability were likewise motivated by such comparisons. However a major difficulty is that, while there is a wealth of spatially resolved snapshots of giant planet atmospheres, there was a dearth of high cadence, full disk multi-band photometry of any planet in the outer Solar System. This led Gelino & Marley (2000), for example, to synthesize an artificial light curve of Jupiter from static optical and thermal infrared images. The last few years has finally seen a new interest in such observations and a number of "Solar System planets as point sources" observations have been obtained by various observatories.

Here we presented full disk observations of an unresolved Neptune by the *Spitzer Space Telescope* and *WISE*. Large amplitude ($\sim$1 mag) variability is detected, likely arising from high contrast, optically thick cloud decks that overlie much of the atmospheric methane opacity. Rotational variability due to bright clouds as seen in Figure 5 are consistent with our $\sim$3 to $\sim$5 μm photometric signal. A similar result came from comparing the time series obtained by the *K*2 mission with *HST* images. Large scale cloud features evolve in height, size, and overall contrast, and they appear and disappear at different latitudes. The single *Spitzer* visit to the planet reported on here was insufficient to detect such evolution. A longer, systematic sampling of the ice giant lightcurves by *Spitzer* accompanied by disk resolved imaging by *HST* would provide an outstanding dataset for comparative studies of weather in substellar objects.

This work is based on observations made with the *Spitzer* Space Telescope, which is operated by the Jet Propulsion Laboratory (JPL), California Institute of Technology (Caltech), under a contract with the National Aeronautics and Space Administration (NASA). Support for this work was provided by NASA through an award issued by JPL/Caltech.

This publication makes use of data products from *WISE*, which is a joint project of the University of California, Los Angeles, and JPL/Caltech, funded by the NASA. This research has made use of the NASA/IPAC Infrared Science Archive, which is operated by JPL/Caltech, under contract with NASA.

This publication makes use of data products from the NASA/ESA *Hubble Space Telescope*, under programs GO13937 and GO14492, which is operated by the Association of Universities for Research in Astronomy, Inc., under NASA contract NAS5-26555, with special thanks to the GO14492 science team (M.H. Wong, A.A. Simon, I. de Pater, J.W. Tollefson, K. de Kleer, H.B. Hammel, S. Cook, R. Hueso, A. Sánchez-Lavega, M. Delcroix, L. Sromovsky, G. Orton, and C. Baranec).

This research was carried out in part at JPL/Caltech under a contract with NASA and with the support of the NASA Origins of Solar Systems program via grant 11-OSS11-0074.

Facilities: Spitzer, *Kepler*, *HST*.

REFERENCES

Ackerman, A. S., & Marley, M. S. 2001, ApJ, 556, 872
Apai, D., Radigan, J., Buenzli, E., et al. 2013, ApJ, 768, 121
Apai, D., Schneider, G., Grady, C., et al. 2016, ApJ, 820, 40
Bean, J. L., Désert, J.-M., Kabath, P., et al. 2011, ApJ, 743, 92
Berta, Z. K., Charbonneau, D., Désert, J.-M., et al. 2012, ApJ, 747, 35
Buenzli, E., Apai, D., Morley, C., et al. 2012, ApJ, 760, 31
Burrows, A., Sudarsky, D., & Lunine, J. I. 2003, ApJ, 596, 587
Conrath, B. J., Flasar, F. M., & Gierasch, P. J. 1991, JGR, 96, 18931
Cushing, M. C., Hardegree-Ullman, K., Trucks, J., et al. 2016, ApJ, 823, 152
Cushing, M. C., Roellig, T. L., Marley, M. S., et al. 2006, ApJ, 648, 614
Cutri, R. M., Wright, E. L., Conrow, T., et al. 2012, http://wise2.ipac.caltech.edu/docs/release/allsky/expsup/
Faherty, J., Tinney, C., Skemer, A., & Monson, A. 2014, ApJL, 793, L16
Fazio, G., Hora, J., Allen, L., et al. 2004, ApJS, 154, 10
Fletcher, L. N., de Pater, I., Orton, G. S., et al. 2014, Icar, 231, 146
Fortney, J. J. 2005, MNRAS, 364, 649
Gelino, C., & Marley, M. 2000, in ASP Conf. Ser. 212, From Giant Planets to Cool Stars, ed. C. A. Griffith & M. S. Marley (San Francisco, CA: ASP), 322
Gillon, M., Triaud, A., Jehin, E., et al. 2013, A&A, 555, L5
Gizis, J., Dettman, K., Burgasser, A., et al. 2015, ApJ, 813, 104
Hammel, H., & Lockwood, G. 2007, Icar, 129, 466
Hammel, H. B., Sitko, M. L., Lynch, D. K., et al. 2007, AJ, 134, 637
Howell, S., Sobeck, C., Haas, M., et al. 2014, PASP, 126, 398
Ingalls, J. G., Krick, J. E., Carey, S. J., et al. 2012, Proc. SPIE, 8442, 84421Y
Ingalls, J. G., Krick, J. E., Carey, S. J., et al. 2016, AJ, 152, 44
Irwin, P., Fletcher, L., Tide, D., et al. 2016, Icar, 271, 418
Karkoschka, E. 2011, Icar, 215, 439
Lockwood, G. W., Thompson, D. T., Lutz, B. L., & Howell, E. S. 1991, ApJ, 368, 287
Luhman, K., & Esplin, T. 2016, AJ, in press, arXiv:1605.06655
Mainzer, A., Cushing, M. C., Skrutskie, M., et al. 2011, ApJ, 726, 30
Marley, M. S., Ackerman, A. S., Cuzzi, J. N., & Kitzmann, D. 2013, in Comparative Climatology of Terrestrial Planets, ed. S. J. Mackwell et al. (Tucson, AZ: Univ. Arizona Press), 367
Metchev, S., Heinze, A., Apai, D., et al. 2015, ApJ, 799, 154
Orton, G., Encrenaz, T., Leyrat, C., et al. 2007, A&A, 473, L5
Orton, G., Fletcher, L., Liu, J., et al. 2012, P&SS, 61, 161
Pont, F., Knutson, H., Gilliland, R. L., Moutou, C., & Charbonneau, D. 2008, MNRAS, 385, 109
Radigan, J. 2014, ApJ, 797, 120
Reach, W. T., Megeath, S. T., Cohen, M., et al. 2005, PASP, 117, 978
Simon, A., & Beebe, R. 1996, Icar, 121, 319
Simon, A. A., Rowe, J. F., Gaulme, P., et al. 2016, ApJ, 817, 162
Smith, B., Soderblom, L., Banfield, C., et al. 1989, Sci, 246, 1422
Sromovsky, L. A., Fry, P. M., Baines, K. H., & Dowling, T. E. 2001, Icar, 149, 435
Tollefson, J. W., de Pater, I., Marcus, P. S., et al. 2016, Icar, in press
Werner, M., Roellig, T., Low, F., et al. 2004, ApJS, 154, 1
Westphal, J. A. 1969, ApJL, 157, L63
Wong, M. H., Fry, P. M., & Simon, A. A. 2016, CBET, #4278 (http://www.cbat.eps.harvard.edu/iau/cbet/004200/CBET004278.txt)
Wright, E. L., Eisenhardt, P. R. M., Mainzer, A. K., et al. 2010, AJ, 140, 1868
Yang, H., Apai, D., Marley, M., et al. 2015, ApJL, 798, L13
Yang, H., Apai, D., Marley, M., et al. 2016, ApJ, 826, 8
Zhou, Y., Apai, D., Schneider, G., et al. 2016, ApJ, 818, 176